Determination of the $2s^22p^5 - 2s2p^6$ transition energy in fluorine-like nickel utilizing a low-lying dielectronic resonance

S. X. Wang,[1] Z. K. Huang,[2] W. Q. Wen,[2,3,*] W. L. Ma,[1] H. B. Wang,[2] S. Schippers,[4,5] Z. W. Wu,[6] Y. S. Kozhedub,[7] M. Y. Kaygorodov,[7] A. V. Volotka,[8] K. Wang,[9] C. Y. Zhang,[10] C. Y. Chen,[10] C. Liu,[1] H. K. Huang,[2,3] L. Shao,[2] L. J. Mao,[2,3] X. M. Ma,[2] J. Li,[2] M. T. Tang,[2] K. M. Yan,[2] Y. B. Zhou,[2] Y. J. Yuan,[2,3] J. C. Yang,[2,3] S. F. Zhang,[2,3] X. Ma,[2,3,†] and L. F. Zhu[1,‡]

[1]*Department of Modern Physics, University of Science and Technology of China, Hefei, Anhui 230026, China*
[2]*Institute of Modern Physics, Chinese Academy of Sciences, Lanzhou 730000, China*
[3]*University of Chinese Academy of Sciences, Beijing 100049, China*
[4]*I. Physikalisches Institut, Justus-Liebig-Universität Gießen, 35392 Giessen, Germany*
[5]*Helmholtz Forschungsakademie Hessen für FAIR, Campus Giessen, 35392 Giessen, Germany*
[6]*Key Laboratory of Atomic and Molecular Physics & Functional Materials of Gansu Province, College of Physics and Electronic Engineering, Northwest Normal University, Lanzhou 730070, China*
[7]*Department of Physics, St. Petersburg State University, Universitetskaya 7/9, 199034 St. Petersburg, Russia*
[8]*School of Physics and Engineering, ITMO University, Kronverkskiy prospekt 49, 197101 St. Petersburg, Russia*
[9]*Hebei Key Lab of Optic-Electronic Information and Materials, The College of Physics Science and Technology, Hebei University, Baoding 071002, China*
[10]*Shanghai EBIT Laboratory, Institute of Modern Physics, Fudan University, Shanghai 200433, China*

(Received 27 May 2022; accepted 19 September 2022; published 13 October 2022)

High-precision spectroscopy of the low-lying dielectronic resonances in fluorine-like Ni^{19+} ions was studied by employing the electron-ion merged-beams method at the heavy-ion storage ring CSRm. The measured dielectronic-recombination (DR) resonances are identified by comparison with relativistic calculations utilizing the flexible atomic code. The lowest-energy resonance at about 86 meV is due to DR via the $(2s2p^6[^2S_{1/2}]6s)_{J=1}$ intermediate state. The position of this resonance could be determined within an experimental uncertainty of as low as ± 4 meV. The binding energy of the 6*s* Rydberg electron in the resonance state was calculated using two different approaches, the multiconfigurational Dirac-Hartree-Fock (MCDHF) method and the stabilization method (SM). The sum of the experimental $(2s2p^6[^2S_{1/2}]6s)_{J=1}$ resonance energy and the theoretical 6*s* binding energies from the MCDHF and SM calculations yields the following values for the $2s^22p^5\,^2P_{3/2} \rightarrow 2s2p^6\,^2S_{1/2}$ transition energy: $149.056(4)_{\mathrm{exp}}(20)_{\mathrm{theo}}$ and $149.032(4)_{\mathrm{exp}}(6)_{\mathrm{theo}}$, respectively. The theoretical calculations reveal that second-order QED and third-order correlation effects contribute together about 0.1 eV to the total transition energy. The present precision DR spectroscopic measurement builds a bridge which enables comparisons between different theories.

DOI: 10.1103/PhysRevA.106.042808

I. INTRODUCTION

Atomic energy levels of highly charged ions (HCIs) are ideal systems for testing the quantum electrodynamics (QED) and relativistic effects [1,2]. Electron-beam ion traps [3–5] and heavy-ion storage rings [6–8] offer unique opportunities for precision studies with HCI. In particular, heavy-ion storage rings equipped with an electron cooler serve as ideal platforms for electron-ion merged-beams experiments. This technique has been intensively employed at the TSR at the Max Planck Institute for Nuclear Physics (MPIK) in Heidelberg [9,10], the CRYRING at the Manne Siegbahn Laboratory (MSL) in Stockholm [11] (in 2013 relocated to GSI in Darmstadt [7]), and the Experimental Storage Ring (ESR) at GSI [12,13]. More recently, the experimental approach was also implemented at the ion-storage rings HIRFL-CSRm and CSRe at the Institute of Modern Physics (IMP), Chinese Academy of Sciences, and already delivered results on electron-ion recombination of a number of ion species [14–16]. Here it is used for a precise determination of the $2s^22p^5\,^2P_{3/2} \rightarrow 2s\,2p^6\,^2S_{1/2}$ transition energy in F-like Ni^{19+} ions.

The traditional approach to atomic precision spectroscopy of HCI is x-ray spectroscopy, which has been widely used for testing QED predictions concerning the atomic structure of HCI (see, e.g., [17–20]). In a joint experimental and theoretical effort, Lindroth *et al.* [21] demonstrated that QED contributions to atomic transition energies can also be tested by electron-ion collision spectroscopy at a heavy-ion storage

*wenweiqiang@impcas.ac.cn
†x.ma@impcas.ac.cn
‡lfzhu@ustc.edu.cn

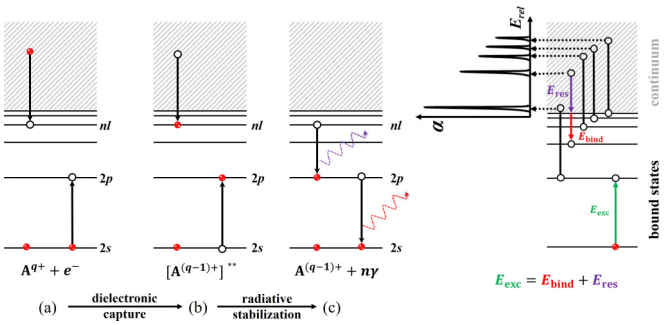

FIG. 1. Left: Schematic diagram of the DR process. The step (a) → (b) represents a dielectronic capture: a free electron is resonantly captured into a Rydberg shell with simultaneous excitation of an inner electron. The step (b) → (c) depicts the subsequent radiative stabilization: the multiply excited intermediate state stabilizes via photon emission. Right: By energy conversation the core excitation energy $E_{\rm exc}$ equals the sum of the Rydberg electron's binding energy $E_{\rm bind}$ and the DR resonance energy $E_{\rm res}$. The α vs. $E_{\rm rel}$ curve represents a made-up DR spectrum that illustrates the principle of how a merged-beams DR rate coefficient α results from a scan of the electron-ion collision energy $E_{\rm rel}$ in the electron-ion center-of-mass frame.

ring, where an electron-ion merged-beams arrangement is employed for measuring low-energy dielectronic recombination (DR) resonances with high experimental resolving power. Moreover, electron-ion collision spectroscopy provides access to nondipole transitions, which usually cannot easily be studied by optical spectroscopy [22].

In the DR process, a free electron is resonantly captured into a Rydberg state with simultaneous excitation of an inner electron (dielectronic capture, Fig. 1). If the thus-formed intermediate multiply excited state decays radiatively the DR process will be completed (radiative stabilization). The measured DR resonance energies $E_{\rm res}$ correspond to the energies of the associated doubly excited states with respect to the first ionization energy of the recombining ion's initial level. As depicted in Fig. 1, the core-excitation energy $E_{\rm exc}$ of the recombining ion can be obtained as

$$E_{\rm exc} = E_{\rm res} + E_{\rm bind}, \tag{1}$$

where $E_{\rm bind}$ is the absolute value of the Rydberg electron binding energy. For sufficiently high principal quantum numbers n of the Rydberg electron the later quantity can be calculated to a high accuracy, e.g., in the framework of relativistic many-body perturbation theory (RMBPT) [21,23]. In principle, if several resonances of a Rydberg series are measured, $E_{\rm bind}$ can be extrapolated to zero by extrapolating $n \to \infty$ such that no separate calculation of $E_{\rm bind}$ is required [24,25]. In the present work, however, we employ the joint experimental and theoretical approach similar to what was used in earlier studies [21,23,26,27].

As a consequence of the merged-beams kinematics, the experimental resolving power of electron-ion merged-beams experiments is highest at the lowest energies (see, e.g., [28]). At the same time, the uncertainty of the experimental electron-ion collision energy scale is lowest at zero collision energy (see, e.g., [25]). Therefore, work on precision electron-ion collision spectroscopy concentrated on measuring low-energy DR resonances.

In [21], the $4p_{1/2} - 4s_{1/2}$ transition energy in copper-like Pb^{53+} was determined to be $E_{\rm exc} = 118.101 \pm 0.001$ eV from measured DR resonances at $E_{\rm res} \lesssim 40$ meV with an uncertainty of only ± 1 meV, corresponding to an accuracy of 8.5 ppm. In a follow-up study, Madzunkov *et al.* [26] investigated the $2p_{1/2} - 2s_{1/2}$ transition in Li-like Kr^{33+}. An uncertainty of ± 8 meV was obtained for the transition energy. This comparatively large value was due to the fact that the lowest-energy DR resonances of this ion appear only above about 5 eV. At the TSR, the $2p_{3/2} - 2s_{1/2}$ transition energy in Li-like Sc^{18+} could be determined to within ± 2 meV [27] from DR resonances in the electron-ion collision energy range 30–70 meV. Later, Lestinsky *et al.* [23] reduced this uncertainty by more than an order of magnitude by using an internally cold electron beam from a liquid-nitrogen-cooled photocathode [29]. Their result probed few-body effects on radiative corrections on the 1% level. Moreover, the experimentally achieved resolving power allowed for the observation of the hyperfine splitting of the $1s^2\,2s\ ^2S_{1/2}$ ground level.

Here, we present a precision-spectroscopy measurement with a more complex system than the previously studied Li-like ions, i.e., fluorine-like $^{58}Ni^{19+}$. As already reported in [16], we measured the merged-beams rate coefficient for DR of $^{58}Ni^{19+}$ ions in the energy of 0-160 eV, including all the DR resonances associated with $2s \to 2p$ core excitations ($\Delta N = 0$ DR):

$$\begin{aligned} &{}^{58}Ni^{19+}(2s^2 2p^5[^2P_{3/2}]) + e^- \\ &\quad \to \begin{cases} {}^{58}Ni^{18+}(2s^2 2p^5[^2P_{1/2}]nl)^{**} \to {}^{58}Ni^{18+} + \gamma, \\ {}^{58}Ni^{18+}(2s\,2p^6[^2S_{1/2}]nl)^{**} \to {}^{58}Ni^{18+} + \gamma. \end{cases} \end{aligned} \tag{2}$$

The lowest-energy $(2s\,2p^6[^2S_{1/2}]\,6s)_{J=1}$ resonance occurs at ~86 meV. The currently recommended value for the associated $2s^2 2p^5\ ^2P_{3/2} - 2s\,2p^6\ ^2S_{1/2}$ core-transition energy is 149.05 ± 0.12 eV [30]. The results of the above-described previous electron-ion collision-spectroscopic works suggested that the uncertainty of this value can be much reduced to a few meV, provided the binding energy of the 6*s* Rydberg electron can be evaluated to an even better accuracy. This would offer an opportunity for a sensitive test of second-order QED contributions to electron binding energies in fluorine-like nickel. We mention that previous work on the $2s^2 2p^5\ ^2P_{3/2} - 2s\,2p^6\ ^2S_{1/2}$ transition in Ni^{19+} was carried out using various experimental [31–33] and theoretical [34–39] approaches, partly addressing atomic-data needs in fusion-plasma physics and astrophysics.

The present paper is organized as follows. The experimental procedure is presented in Sec. II with a detailed discussion of the data-reduction procedures and the error analysis. In Sec. III, we present a general description of the theoretical treatment. The experimental results are then discussed in Sec. IV. Finally, Sec. V provides a conclusive summary.

II. EXPERIMENT

A. Measurement procedure

The experiment was performed by employing the electron-ion merged-beams technique at the heavy-ion storage ring CSRm at the Institute of Modern Physics in Lanzhou, China. Several DR measurements related to astrophysical and plasma applications were carried out successfully at the CSRm [14–16] since the calibration experiment with lithium-like Ar^{15+} in 2015 [14]. Recombination rate-coefficients of fluorine-like nickel were already published previously in Ref. [16], which also contains a detailed description of the experimental setup and procedures. Here we focus on the precise evaluation of the resonance energies of the lowest-energy DR resonances.

In the present measurement, the $^{58}Ni^{19+}$ ion beam from a superconducting electron cyclotron resonance ion source [40] was accelerated by a sector-focused cyclotron and then injected into the storage ring at an energy of 6.15 MeV/u. The stored ion beam reached a maximum current of 80 μA after the injection pulses, corresponding to 3.7×10^8 stored ions. The circulating ion beam passed millions of times per second through the 4-m-long electron-ion interaction region. In the electron cooler, the electron beam was magnetically guided to prevent it from diverging. The magnetic fields at the cathode and the cooler section were 125 mT and 39 mT, respectively. Thereby, the transverse electron beam energy spread was reduced by adiabatically passing from the higher magnetic field in the cathode to the lower magnetic field in the cooler section [41]. In the electron-ion interaction region, the expanded electron beam had a diameter of 62 mm and a particle density of 7.1×10^6 cm^{-3}. By electron-beam profile measurements [42] we verified that a uniform beam density distribution was achieved in the present measurements. The longitudinal electron energy-spread was largely reduced by accelerating the electrons to the cooling energy, where the electrons moved as fast as the stored ions.

The electron velocity-distribution can be characterized by the transverse (with respect to the electron-beam direction) and longitudinal temperatures $T_\parallel$ and $T_\perp$ [43]

$$f(\vec{v}, v_d) = \left(\frac{m_e}{2\pi k T_\parallel}\right)^{1/2} \exp\left[-\frac{m_e (v_\parallel - v_d)^2}{2kT_\parallel}\right] \times \frac{m_e}{2\pi k T_\perp} \exp\left(-\frac{m_e v_\perp^2}{2kT_\perp}\right). \quad (3)$$

The distribution is termed *flattened Maxwellian* due to the fact that $T_\parallel \ll T_\perp$. Its anisotropy leads to asymmetric DR resonance line shapes as discussed in more detail below. In Eq. (3), v_d corresponds to the energy detuning applied to the electron beam. $v_\parallel$ and $v_\perp$ are the longitudinal and perpendicular components of the electron velocity $\vec{v}$. The electron-energy spread that results from Eq. (3) can be calculated as [28]

$$\Delta E_{\rm rel} = \sqrt{(\ln 2 k_B T_\perp)^2 + 16 \ln 2 k_B T_\parallel E_{\rm rel}}, \quad (4)$$

where $E_{\rm rel}$ denotes the electron-ion collision energy in the electron-ion center-of-mass frame. It is evident that the lowest-energy resonances can be measured with the highest resolving power.

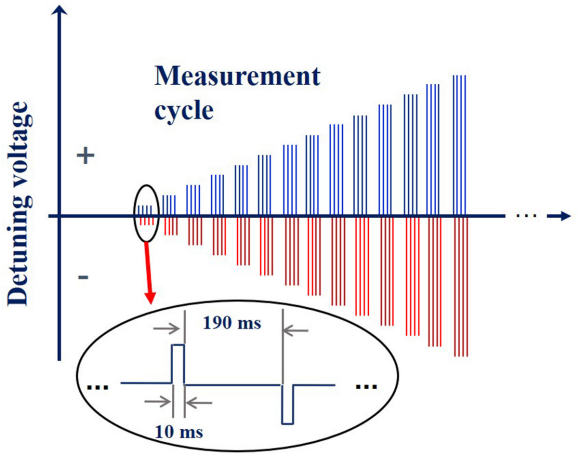

FIG. 2. Illustration of the timing sequence of detuning voltages in the present measurement. The voltage was incremented volt by volt only after each injection, i.e., we only measured recombined ions at a single detuning voltage during each injection-measurement cycle to collect a statistically significant number of counts.

The injected ion beam was cooled by the Coulomb interaction with the cold electrons inside the electron cooler [44]. At cooling, the electrons and the ions shared the same average velocity in the laboratory frame, corresponding to zero electron-ion collision energy in the center-of-mass frame. The cooling phase at the beginning of each injection-measurement cycle lasted for 2 s. In the ensuing electron-ion recombination measurements, the cold electrons acted as an electron target. Nonzero electron-ion collision energies were realized by fast detuning the electron beam energy away from the cooling energy. The electron beam energy was controlled by a specially designed detuning system, which is capable of switching quickly between the cooling voltage and positive or negative detuning voltages as illustrated in Fig. 2. After every 10 ms of detuning, the ion beam was cooled again for 190 ms to keep the beam quality. The recombined ions with a changed charge state lowered by one unit were separated from the primary ion beam in the dipole magnet downstream from the electron cooler and detected by a movable scintillation particle-detector (YAP: Ce + PMT) with nearly 100% efficiency [45]. A sketch of the electron cooler and the particle detector is presented in Fig. 3. The ion current and the revolution frequency were monitored by a DC current transformer and a Schottky spectrum-analyzer [46], respectively.

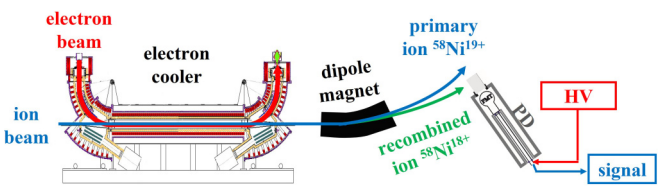

FIG. 3. Sketch of the experimental arrangement at the CSRm electron cooler. The scintillation particle-detector was appropriately placed behind the dipole magnet downstream of the electron cooler for stopping and counting the recombined ions.

B. Data reduction

The absolute recombination rate coefficient $\alpha(E)$ at the electron-ion collision energy $E_{\rm rel}$ was obtained by normalizing the recorded count rates $R(E_{\rm rel})$ to the measured electron and ion currents [47]

$$\alpha(E_{\rm rel}) = \frac{R(E_{\rm rel})}{N_i n_e (1-\beta_e\beta_i)}\frac{C}{L}, \tag{5}$$

where N_i is the number of the stored ions and n_e is the electron density, which is virtually independent of the electron energy over the narrow energy range considered in this work. The subscripts e and i represent the electron and ion beams respectively. The quantities $C = 161.0\,\text{m}$ and $L = 4.0\,\text{m}$ are the circumference of the ring and the effective interaction length. β_e and β_i are the velocity factors of the electron and ion beams, respectively. The electron-ion collision energy in the center-of-mass frame was calculated as [48]

$$E_{\rm rel} = m_i c^2(1+\mu)\left[\sqrt{1+\frac{2\mu}{(1+\mu)^2}(G-1)}-1\right], \tag{6}$$

with the electron-ion mass-ratio $\mu = m_e/m_i$,

$$G = \gamma_e\gamma_i - \sqrt{(\gamma_e^2-1)(\gamma_i^2-1)}\cos\theta, \tag{7}$$

$\gamma_{e,i} = (1-\beta_{e,i}^2)^{-1/2}$, and the angle θ between the two beams in the laboratory frame.

The recombined ion counts and the related parameters were stored each millisecond and the recorded data from the centers of the detuning periods were taken for deriving the rate coefficient in the data processing. The original spectra of the ion counts as a function of the detuning voltages up to $\pm 150\,\text{V}$ are presented Fig. 4(a). The data displayed in Fig. 4(b) resulted from transforming the detuning voltages into electron-ion collision energies via Eq. (6) and the count rates into rate coefficients via Eq. (5). It should be noted that, in addition to DR resonances, the displayed rate coefficient also contains a contribution by nonresonant radiative recombination (RR, discussed below) that decreases sharply with increasing $|E|$, as well as a practically constant background resulting from charge-changing collisions with residual-gas particles.

Figure 5 presents the background-subtracted experimental electron-ion recombination spectrum of $^{58}Ni^{19+}$ ions in the energy range of 0–14 eV together with a theoretical result that we obtained by using the flexible atomic code (FAC) [49]. For comparison, the calculated DR cross sections were convoluted with the experimental electron beam velocity distribution [Eq. (3)]. There is a good agreement with the measured data. Minor discrepancies are likely to be attributed to an approximate treatment of electron correlation effects in the calculation. The inset magnifies the resonances below 1 eV and the labeled vertical bars mark the calculated DR resonance positions. DR via $2s\,2p^6[^2S_{1/2}]6s$ and $2s^22p^5[^2P_{1/2}]17l$ intermediate levels are the dominant channels in this energy range. Due to the limited experimental resolution the associated fine-structure splittings are generally not fully resolved in the present measurement. However, an isolated resonance occurs at about 86 meV on top of the steeply decreasing

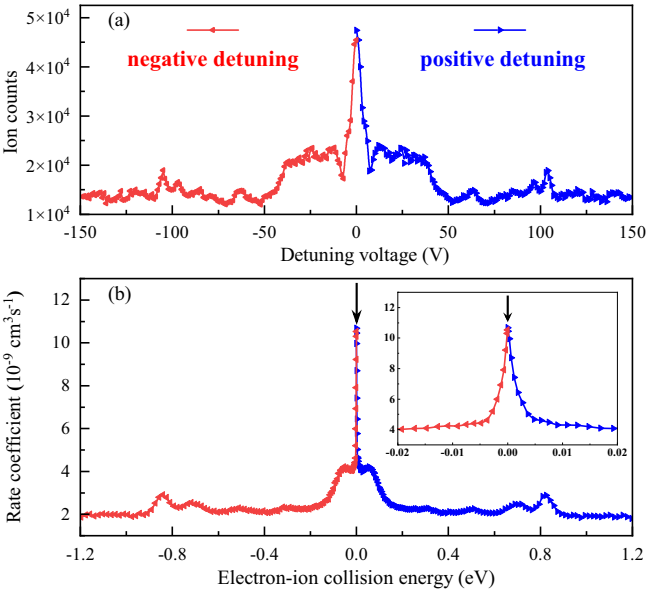

FIG. 4. (a) The original recorded recombined ion counts for detuning voltages up to $\pm 150\,\text{V}$. (b) The derived rate coefficients for the corresponding electron-ion collision energies ranging from $-1.2\,\text{eV}$ to $+1.2\,\text{eV}$. The negative sign refers to collision energies that result from negative detuning voltages. The inset highlights the recombination rate-coefficient near zero electron-ion collision energy.

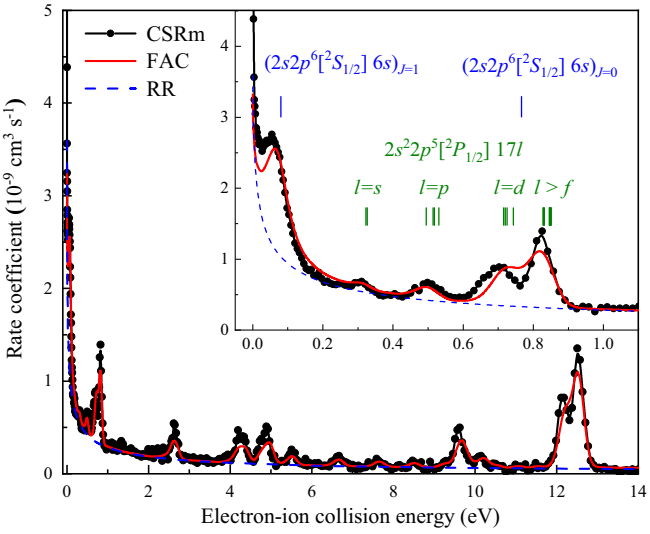

FIG. 5. Experimental electron-ion recombination spectrum (black symbols) in comparison with the result of theoretical calculations. The blue dashed line is the RR rate coefficients and the red full line is calculated DR rate coefficients using the FAC code superimposed on the calculated RR. The inset enlarges the low-energy resonances with their calculated resonance positions indicated by the vertical bars. The first resonance marked as $(2s2p^6[^2S_{1/2}]6s)_{J=1}$ indicates that the intermediate state has a total momentum $J = 1$, which is formed when the free electron is captured into the $6s$ shell and the initial ion is excited into the $2s2p^6[^2S_{1/2}]$ state.

RR rate coefficient. It is attributed to the $(2s\,2p^6[^2S_{1/2}]6s)_{J=1}$ intermediate level.

C. Uncertainty of the energy scale

According to Eq. (6), the accuracy of the electron-ion collision energy depends on the Lorentz factors of the electron and ion beams as well as on the angles between the two beams. The Lorentz factor of the ion beam is

$$\gamma_i = 1 + \frac{E_i}{m_i c^2}, \tag{8}$$

where E_i and m_i are the ion kinetic energy and the ion mass, respectively. The energy equivalent of the latter can be calculated as $m_i c^2 \approx A m_u c^2 - 19 m_e c^2$, which neglects the contributions from the electron binding energies. Using $A = 57.9353424$ for the atomic mass of the ^{58}Ni atom [50] and $m_e c^2/m_u c^2 = 5.48579909\times10^{-4}$ for the electron mass in atomic mass units [51] one arrives at $m_i c^2 \approx 57.92492 m_u c^2$.

The Lorentz factor of the electron beam can be calculated from the cooler-cathode voltage U_c, the space-charge potential U_s of the electron beam, and the detuning voltage U_d as

$$\gamma_e = 1 + \frac{e(U_c + U_s + U_d)}{m_e c^2}. \tag{9}$$

At cooling, electrons and ions move with the same velocity such that $\gamma_i = \gamma_e$ for $U_d = 0$. The ion energy can be thus expressed as $E_i = e(U_c + U_s)m_i/m_e$ and the Lorentz factor of the ion beam can be written as

$$\gamma_i = 1 + \frac{e(U_c + U_s)}{m_e c^2}. \tag{10}$$

Neglecting the uncertainties of the particle masses, the uncertainty $\Delta E_{\rm rel}$ of the electron-ion collision energy [Eq. (6)] thus depends on the uncertainty ΔE_d of the detuning energy $E_d = eU_d$, the uncertainty ΔE_0 of the cooling energy $E_0 = e(U_c + U_s)$, and the uncertainty $\Delta\theta$ of the angle θ, i.e.,

$$(\Delta E_{\rm rel})^2 = \left|\frac{\partial E_{\rm rel}}{\partial \gamma_i}\right|^2 \left(\frac{\Delta E_0}{m_e c^2}\right)^2 + \left|\frac{\partial E_{\rm rel}}{\partial \varepsilon_d}\right|^2 \left(\frac{\Delta E_d}{m_e c^2}\right)^2 + \left|\frac{\partial E_{\rm rel}}{\partial \theta}\right|^2 (\Delta\theta)^2. \tag{11}$$

The partial derivatives in Eq. (11) can be straightforwardly calculated after substituting $\gamma_e = \gamma_i + \varepsilon_d$ in Eq. (7) with $\varepsilon_d = E_d/(m_e c^2)$.

The cooling energy can be obtained from the cathode voltage and the space charge potential. Both values bear considerable uncertainties. The cathode voltage can be read from the power supply with an uncertainty of 0.5%. The space charge potential and its uncertainty are even less accessible since U_s cannot be measured directly, although its influence on the ion beam can be monitored by the Schottky beam analysis. In this situation we determined the ion energy and, thus, the cooling energy $E_0 = E_i m_e/m_i$ from the magnetic rigidity of the storage ring's dipole magnets, which keep the ions on a closed orbit. The associated uncertainty results in a relative uncertainty $\Delta E_0/E_0 = 0.005$. We also point out that an accurate value of the cooling energy is required for obtaining recombination spectra that are symmetric about $E_{\rm rel} = 0$ on the electron-ion collision-energy scale (Fig. 4).

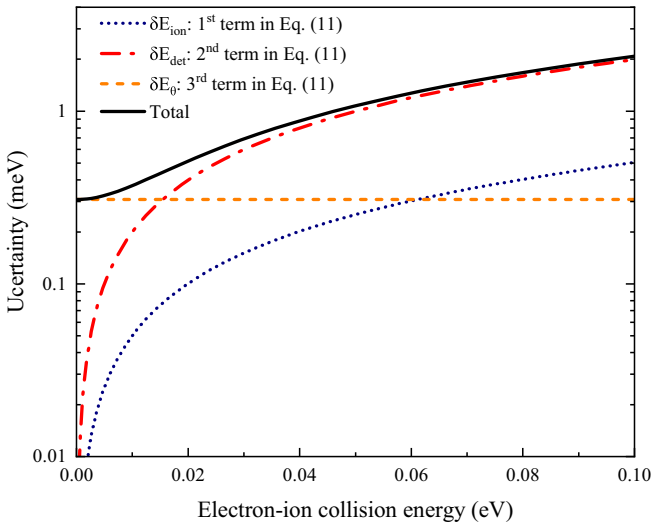

FIG. 6. Systematic uncertainties of the electron-ion collision-energy scale. The individual contributions [corresponding to the terms in Eq. (11)] are summed quadratically to obtain the total uncertainty. At the position of the lowest-energy DR resonance at 86 meV amounts to 2.0 meV (Table I).

The known Rydberg series limit of the $2s\,2p^6[^2S_{1/2}]nl$ DR resonances at 149.05 ± 0.12 eV [30] provides another calibration point of the energy scale. We applied a 2% correction to the nominal collision energy scale to achieve agreement of the experimental series limit with the known value [16]. The 0.08% relative uncertainty of the known series limit is a lower limit for the uncertainty of the thereby calibrated detuning energies. This calibration to a certain extent also takes care of ion-beam dragging effects that occur at nonzero relative energies, i.e., when $U_d \neq 0$. The dragging effect is caused by the Coulomb interaction between the electron and ion beams, which results in a force on the ion beam trying to pull the ions to the current electron beam velocity [27,52]. It should be noted that the presently applied measurement mode (Fig. 2) with alternatingly negative and positive detuning energies applied for only short time intervals and considerably longer intervening cooling time intervals was deliberately chosen to minimize the drag-force effect. During the measurement, the Schottky spectrum also showed no evident signals of dragging. To account for possible nonlinearities of the U_d power supply and the drag-force effect we conservatively assumed a 1% relative uncertainty for the detuning energy, i.e., $\Delta E_d/E_d = 0.01$.

The angle θ between the ion beam and the electron beam was adjusted to 0 as best as achievable by using correction coils that are available at the cooler. The remaining uncertainty is estimated to be 0.3 mrad. Since $\partial E_{\rm rel}/\partial\theta \propto \sin\theta$ one obtains a zero error for $\theta = 0$ from this derivative. Therefore, we calculated the contribution of $\Delta\theta$ to the error budget as the difference $E_{\rm rel}(\gamma_i, \varepsilon_d, \theta = 0.3\,{\rm mrad}) - E_{\rm rel}(\gamma_i, \varepsilon_d, \theta = 0)$.

Figure 6 visualizes the individual contributions to the total uncertainty which correspond to the summands on the right-hand side of Eq. (11). Numerical values for these uncertainties at the position of the lowest-energy DR resonance are given in Table I. The total systematic uncertainty of the resonance

TABLE I. Systematic experimental uncertainties of the electron-ion collision energy 86 meV, i.e., at the position of the lowest-energy DR-resonance (Fig. 5).

	$\Delta E_{\rm rel}$ (meV)
Angle between beams	0.31
Detuning voltage	1.69
Ion beam energy	0.43
Energy calibration	0.86
Total (quadratic sum)	1.97

position is slightly less than 2 meV. Additional statistical and fitting uncertainties will be discussed below.

III. THEORETICAL TREATMENT

A. MCDHF calculation

The $2s^22p^5[^2P_{3/2}] \rightarrow 2s2p^6[^2S_{1/2}]$ transition energy and the binding energy of the $6s$ electron in the $2s2p^6[^2S_{1/2}]6s$ state are calculated by using the relativistic atomic structure package GRASP2018 [53], which was developed based on the multiconfigurational Dirac-Hartree-Fock (MCDHF) method [54,55]. In this method, an atomic-state wave function with a specific parity P, total angular momentum J, and its projection M on the quantization axis is approximated by a set of configuration-state wave functions (CSFs) with the same PJM as follows [54,55]:

$$\psi_\alpha(PJM) = \sum_{r=1}^{n_c} c_r(\alpha)|\phi_r(PJM)\rangle. \tag{12}$$

Here, n_c is the number of the CSFs used. $c_r(\alpha)$ denotes configuration mixing coefficients, which give rise to a representation of the atomic state $|\psi_\alpha\rangle$ in the chosen basis $\{|\phi_r\rangle\}$. The CSFs are initially generated as an antisymmetrized product of a set of orthonormal orbitals and then optimized self-consistently in the basis of the Dirac-Coulomb-Breit Hamiltonian, which is followed by the inclusion of the quantum-electrodynamical effects into the representation $c_r(\alpha)$ of the atomic state $|\psi_\alpha\rangle$ by diagonalizing the Dirac-Coulomb-Breit Hamiltonian matrix. In the calculations of the excitation energy from $2s^22p^5\,[^2P_{3/2}]$ to $2s2p^6\,[^2S_{1/2}]$ in fluorine-like Ni^{19+} ion, all the single and double substitutions from the multireference (MR) configurations (the $2s^22p^5$, $2s2p^6$, $2s^22p^43p$, and $2s2p^53p$) to the active set $\{9s, 9p, 9d, 9f, 9g, 9h, 9i, 9k\}$ are considered, which generate 686 327 CSFs for the block of $J = 3/2$ and odd parity and 274 090 CSFs for the block of $J = 1/2$ and even parity, respectively. Moreover, in obtaining the energy level $(2s2p^6[^2S_{1/2}]6s)_{J=1}$ of neon-like Ni^{18+} ion, all the single and double substitutions from the MR configurations (the $2s2p^65s$, $2s2p^66s$, and $2s2p^67s$) to the active set $\{13s, 13p, 13d, 13f, 13g, 12h, 11i, 10k\}$ are considered, which generate 522 644 CSFs for the block of $J = 1$ and even parity.

In Table II, the total energies (E_h) of the $2s^22p^5\,[^2P_{3/2}]$ and $2s2p^6\,[^2S_{1/2}]$ levels of fluorine-like Ni^{19+} ion and the $(2s2p^6[^2S_{1/2}]6s)_{J=1}$ level of neon-like Ni^{18+} ion are presented as a function of the increasing active set (AS), as well as the transition energies ΔE (eV) for the transitions $2s^22p^5\,{}^2P_{3/2} \rightarrow 2s\,2p^6\,{}^2S_{1/2}$ and $(2s2p^6[^2S_{1/2}]6s)_{J=1} \rightarrow 2s2p^6\,[^2S_{1/2}]$. The MCDHF calculated total energies and ΔE are converged within a few meV with respect to the increasing size of the AS.

B. *Ab initio* calculation

Different theoretical approaches, e.g., the complex coordinate rotation method [56], Feshbach projection operator method, optical potential method, R-matrix method, etc. (see e.g., Ref. [57] and references therein) were proposed to

TABLE II. Total energies (E_h) of the $2s^22p^5\,[^2P_{3/2}]$ and $2s2p^6\,[^2S_{1/2}]$ levels of fluorine-like Ni^{19+} ion and the $(2s2p^6[^2S_{1/2}]6s)_{J=1}$ level of neon-like Ni^{18+} ion are presented as a function of the increasing active set (AS), as well as the transition energies ΔE (eV) for the transitions $2s^22p^5\,{}^2P_{3/2} \rightarrow 2s\,2p^6\,{}^2S_{1/2}$ and $(2s2p^6[^2S_{1/2}]6s)_{J=1} \rightarrow 2s2p^6\,[^2S_{1/2}]$.

	F-like Ni^{19+} (MR = $\{2s^22p^5, 2s2p^6, 2s^22p^43p, 2s2p^53p\}$)		
AO	$E\,(2s^22p^5\,[^2P_{3/2}])$	$E\,(2s2p^6\,[^2S_{1/2}])$	$\Delta E(2s2p^6\,[^2S_{1/2}] \rightarrow 2s^22p^5\,[^2P_{3/2}])$
$\{3s, 3p, 3d\}$	−1292.5833877	−1287.0299079	151.118
$\{4s, 4p, 4d, 4f\}$	−1292.7902178	−1287.3083550	149.169
$\{5s, 5p, 5d, 5f, 5g\}$	−1292.8534402	−1287.3745748	149.088
$\{6s, 6p, 6d, 6f, 6g, 6h\}$	−1292.8806642	−1287.4035955	149.039
$\{7s, 7p, 7d, 7f, 7g, 7h, 7i\}$	−1292.9096358	−1287.4331842	149.022
$\{8s, 8p, 8d, 8f, 8g, 8h, 8i, 8k\}$	−1292.9238447	−1287.4474401	149.020
$\{9s, 9p, 9d, 9f, 9g, 9h, 9i, 9k\}$	−1292.9295149	−1287.4531798	149.019
	Ne-like Ni^{18+} (MR = $\{2s2p^65s, 2s2p^66s, 2s2p^67s\}$)		
AO		$E[(2s2p^6[^2S_{1/2}]6s)_{J=1}]$	$\Delta E[(2s2p^6[^2S_{1/2}]6s)_{J=1} \rightarrow 2s2p^6\,[^2S_{1/2}]]$
$\{8s, 8p, 8d, 8f, 8g, 8h, 8i, 8k\}$		−1292.8391704	158.08
$\{9s, 9p, 9d, 9f, 9g, 9h, 9i, 9k\}$		−1292.8712688	151.37
$\{10s, 10p, 10d, 10f, 10g, 10h, 10i, 10k\}$		−1292.8918299	150.13
$\{11s, 11p, 11d, 11f, 11g, 11h, 11i, 10k\}$		−1292.9022762	149.63
$\{12s, 12p, 12d, 12f, 12g, 12h, 11i, 10k\}$		−1292.9085850	148.99
$\{13s, 13p, 13d, 13f, 13g, 12h, 11i, 10k\}$		−1292.9165405	148.82
$\{14s, 14p, 14d, 14f, 13g, 12h, 11i, 10k\}$		−1292.9277362	148.97

describe the autoionizing states. In the present work, we apply the stabilization method (SM), pioneered by Hazi and coworkers [58,59], utilized in numerous investigations [60–63]. The idea of this method [64] is to diagonalize the Hamiltonian of a quantum system with suitable square-integrable real wave functions and investigate the spectra in the neighborhood of resonance position under small variations of the basis set. It can be done elegantly using the spectral density of states function

$$\rho_n(E) = \left| \frac{\xi_{i+1} - \xi_i}{E_n(\xi_{i+1}) - E_n(\xi_i)} \right|, \tag{13}$$

where ξ_i is the basis variation parameter and $E_n(\xi_i)$ is the energy level near the resonance position. The maximum of the spectra density function ρ_n corresponds to the energy of the resonance state (see, e.g., Ref. [63] for details). Our realization of the approach is based on the configuration-interaction Dirac-Fock-Strum (CI-DFS) method [65–67], where the basis set is varied by the reference energy parameter for Sturm basis orbitals.

The QED calculations of the transition $2s2p^6\ {}^2S_{1/2} \rightarrow 2s^2 2p^5\ {}^2P_{3/2}$ energy in fluorine-like nickel is based on the QED perturbation theory in the extended Furry picture [68], which previously was also employed for the evaluation of the ground-state fine-structure energy in fluorine-like ions [69–72]. The zeroth-order Hamiltonian is defined as

$$H_0 = \int d^3x \psi^\dagger(x)[-i\boldsymbol{\alpha}\boldsymbol{\nabla} + \beta m + V_{\rm C}(\mathbf{x}) + V_{\rm scr}(\mathbf{x})]\psi(x), \tag{14}$$

where α_i and β are the Dirac matrices and $\psi(x)$ is a field operator expanded in terms of the Dirac wave functions $\psi_n(\mathbf{x})$

$$[-i\boldsymbol{\alpha}\boldsymbol{\nabla} + \beta m + V_{\rm C}(\mathbf{x}) + V_{\rm scr}(\mathbf{x})]\psi_n(\mathbf{x}) = \varepsilon_n \psi_n(\mathbf{x}). \tag{15}$$

In Eq. (14), in addition to the nuclear Coulomb potential $V_{\rm C}$ the screening potential $V_{\rm scr}$, which partially accounts for the interelectronic interaction has been added. In our calculations, we employ the core-Hartree and Kohn-Sham potentials.

The perturbation expansion is performed with respect to the interaction Hamiltonian

$$H_{\rm int} = \int d^3x [\bar{\psi}(x) e \gamma^\mu A_\mu(x) \psi(x) - \psi^\dagger(x) V_{\rm scr}(\mathbf{x}) \psi(x)], \tag{16}$$

where $\gamma^\mu = (\beta, \beta\alpha_i)$, $A_\mu(x)$ is a photon field operator. The second term in Eq. (16) corresponds to the subtraction of the counterterm. For constructing the perturbative expansion, we use the two-time Green's function method [73]. In the present calculations, we account entirely for the first-order corrections, which are given by the one-photon exchange and the one-electron self-energy and vacuum polarization diagrams. These diagrams are computed employing the well-known formal expressions, which can be found in, e.g., Refs. [73,74]. The second-order diagrams include the many-electron radiative (so-called screened QED), one-electron two-loop and two-photon exchange corrections. Here, we evaluate only the screened QED correction employing the techniques and methods thoroughly presented in Refs. [69,75–77]. For the one-electron two-loop contribution, we use the hydrogenic values from Ref. [78]. While the two-photon exchange diagrams are taken into account within the Breit approximation and the uncertainty from the missing higher-order correction is estimated to be $\alpha/(8\pi)(\alpha Z)^4/Z^2$ multiplied by a factor of 5.

The terms which were not accounted for by the rigorous QED theory were evaluated within the Breit approximation employing the CI-DFS method. Within this method, the many-electron wave function and the energy of an atom E in the Breit approximation are to be found as solutions of the Dirac-Coulomb-Breit Hamiltonian. Thus, the CI-DFS method is used to calculate the second- and higher-order interelectronic-interaction corrections. Moreover, we evaluated the recoil correction employing the many-body relativistic mass shift Hamiltonian [75,79–82].

IV. RESULTS AND DISCUSSION

The fitted curve of the low-energy DR spectrum is presented in Fig. 7(a). The data points below 10 meV were excluded from the fitting due to the steep rise of the measured rate coefficient towards lower energies (see Ref. [16] for details), which is difficult to account for in the fit. In the fitting procedure, the first resonance was treated as a Lorentzian profile multiplied by a factor of $E_{\rm res}/E_{\rm rel}$ as discussed in Ref. [83], while the remaining resonances were treated as delta functions. The RR cross sections were calculated using the Bethe and Salpeter [84] formula. Note that the semi-empirical formula was feasible for hydrogenic ions, and, thus, a scaling factor was multiplied to the calculated cross sections to modify the data to F-like nickel ion. The scaling factor resulting from the fit was 1.57. The DR and RR cross sections were added together directly since the interference effect can be neglected safely. Moreover, the DR and RR model cross sections were convolved with the electron beam velocity distribution [Eq. (3)] to account for the experimental energy spread. The electron-beam temperatures obtained from the fit are $k_B T_\parallel = 0.56 \pm 0.05$ meV and $k_B T_\perp = 23 \pm 1$ meV.

According to the fit, the position of the lowest-energy resonance was determined to be 85.8 ± 1.2 meV. Its combined systematic and statistical (resulting from the fit) uncertainty is less than 4 meV at a one-sigma confidence level. The fitted resonance positions and strengths are in fair agreement with the FAC calculation (Table III), which assigns the $(2s2p^6[^2S_{1/2}]6s)_{J=1}$ intermediate level to the lowest-energy resonance. In Fig. 7(b), the DR fit results are compared with the background-subtracted experimental data to provide a better view of the DR resonances. The fact that the maxima of the resonances do not coincide with the fitted resonance positions is a consequence of the asymmetry of the electron-velocity distribution [Eq. (3)].

As described in Sec. III, we calculated the binding energy of the 6s electron of the $(2s2p^6[^2S_{1/2}]6s)_{J=1}$ level using the MCDHF and stabilization methods. We find that the large-scale MCDHF calculations do not converge on the binding energy as the active sets are increased. The energy of the autoionizing level turned out to be extremely sensitive to the choice of basis sets because of the near-degeneracy with the continuum. Therefore, our MCDHF value for the

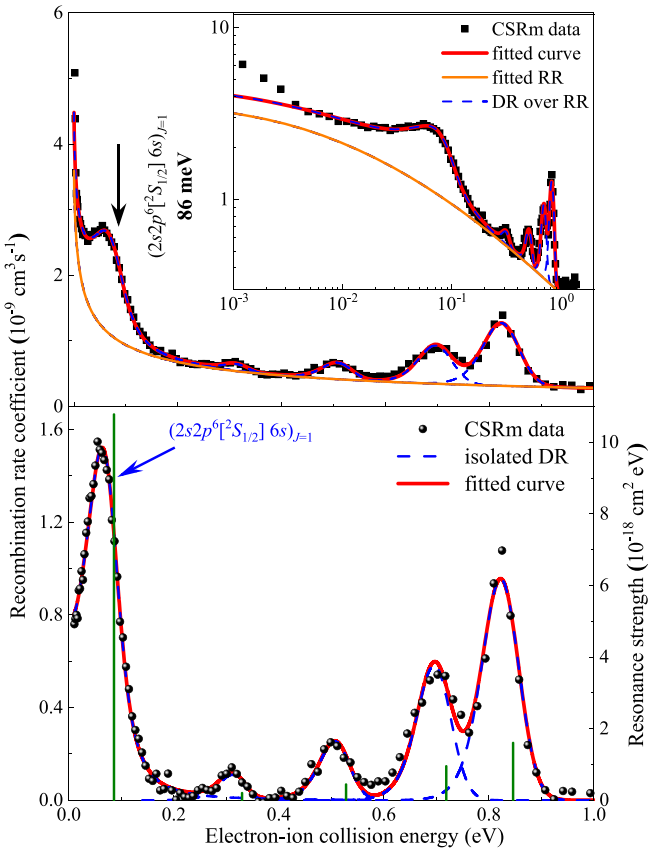

FIG. 7. (a) Fit (red solid line) of the experimental low-energy DR spectrum (black symbols). The fit accounts for isolated DR resonances (blue dashed lines) and the RR rate coefficient (orange solid line). Note that a constant background was subtracted from the data before the curve fit. (b) Experimental DR rate coefficient (symbols) after subtraction of a constant background and the fitted RR contribution along with the fit curve for the DR resonances. The vertical green bars represent the fitted DR resonance positions and strengths. The fitted peak position does not match the resonance maximum due to Eq. (3).

6*s* binding energy of 148.970 eV bears a rather large uncertainty which is estimated to be ±20 meV. The stabilization method exhibits a more favorable convergence behavior. It yields a value of 148.946 ± 0.006 eV for the binding energy of the 6*s* electron. The values for the $2s^22p^5\ ^2P_{3/2} \rightarrow 2s\,2p^6\ ^2S_{1/2}$ transition energy in fluorine-like nickel that results from adding the calculated 6*s* binding energies in the

TABLE III. Experimental and theoretical positions, natural widths, and strengths for the lowest-energy resonance as assigned to the $(2s2p^6[^2S_{1/2}]6s)_{J=1}$ intermediate level. The number in the brackets indicates the experimental uncertainties.

	CSRm	FAC
Resonance position (meV)	86(4)	80
Natural width (meV)	51(5)	56
Resonance strength (10^{-18} eV cm^2)	10.8(1.0)	10.2

TABLE IV. Comparison of the experimental and theoretical results for the $2s^22p^5\ ^2P_{3/2} \rightarrow 2s\,2p^6\ ^2S_{1/2}$ transition energy in fluorine-like nickel ion (in eV). Figures in parentheses represent one-sigma uncertainties.

Method	Energy (eV)
Experiment + theory	
Exp. + MCDHF	$149.056(4)_{\rm exp}(20)_{\rm theo}$
Exp. + SM	$149.032(4)_{\rm exp}(6)_{\rm theo}$
Theory	
MCDHF	149.019(10)
Ab initio	149.046(7)

$(2s2p^6[^2S_{1/2}]6s)_{J=1}$ level and the experimentally derived DR resonance position are listed in Table IV.

Table IV also list the results for the $2s^22p^5\ ^2P_{3/2} \rightarrow 2s\,2p^6\ ^2S_{1/2}$ transition energies of our fully relativistic MCDHF and *ab initio* QED calculations. For this quantity, the large-scale MCDHF calculation yield a convergent value with an uncertainty of ±20 meV when increasing the size of active sets. In the *ab initio* QED calculation, the zeroth-order Dirac result is extended by the correlation corrections evaluated within the Breit approximation, by the first- and second-order QED contributions, as well as by the recoil term. Calculations were performed employing two different starting potentials, core-Hartree and Kohn-Sham. In Table V we present the individual theoretical contributions to the transition $2s^22p^5\ ^2P_{3/2} \rightarrow 2s\,2p^6\ ^2S_{1/2}$ energy in fluorine-like nickel calculated as was explained above in both utilized screening potentials. As one can see from the table, the total results in both potentials perfectly agreeing with each other, although the individual contributions are different. The final uncertainty is dominated by the estimation of the QED effect for the two-photon exchange correction.

Figure 8 compares the present experimentally derived and theoretical results with the previous results from the literature. The determined transition energies agree with the most accurate plasma observation [33] within the error bars. The calculated values by the SUPERSTRUCTURE code [39] and by the coupled cluster method with single and double excitations (CCSD) [36] are significantly larger than our results. The MBPT [34,37] and MCDHF [37] calculations report values for the transition energies without uncertainties,

TABLE V. Individual contributions to the transition $2s^22p^5\ ^2P_{3/2} \rightarrow 2s\,2p^6\ ^2S_{1/2}$ energy in fluorine-like nickel ion (in eV).

Contribution	Core-Hartree	Kohn-Sham
Dirac	123.911	128.743
Correlation (1)	27.190	22.723
Correlation (2)	−1.536	−1.972
Correlation (3)	0.032(2)	0.102(2)
QED (1)	−0.506	−0.510
QED (2)	−0.033(6)	−0.028(6)
Recoil	−0.012(3)	−0.012(3)
Total	149.046(7)	149.046(7)

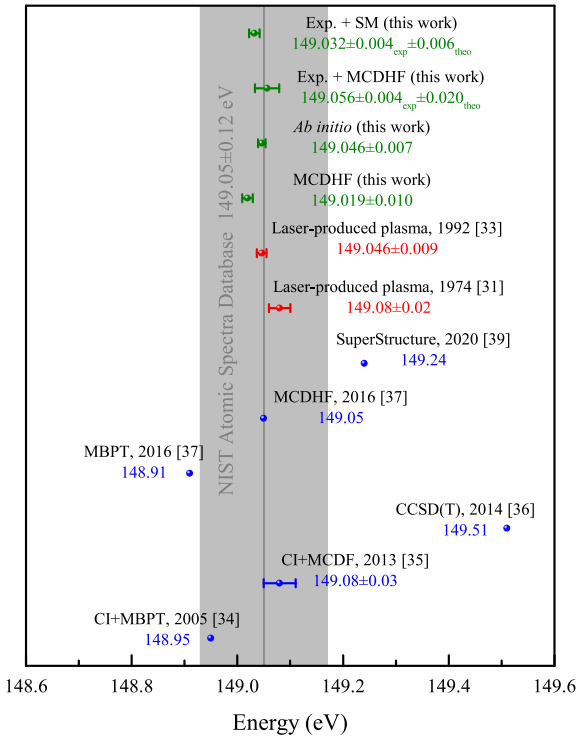

FIG. 8. Available experimental and theoretical transition energies of the $2s^2 2p^5\ ^2P_{3/2} \rightarrow 2s\,2p^6\ ^2S_{1/2}$ along with the present experimentally derived and fully theoretical results. The vertical lines corresponds to the currently recommended value from the NIST Atomic Spectra Database [30]. The gray shaded area marks the associated uncertainty.

which hampers an accurate comparison. The value obtained within the CI-MCDF method [35] agrees well with both our experimental and theoretical results within the given error bars, but our values are more precise. The individual contributions in Table V indicate that third-order correlation effects contribute to at least 0.032(2) eV of the total transition energy. The calculations where the correlation effect was handled with care [34,35,37] yielded values which agree better with the experimental data as compared to the simpler approaches. The MBPT calculations [34,37] are significantly lower than the present data, indicating that the many-body expansion in many-electron systems remains a challenging task.

V. SUMMARY AND OUTLOOK

Electron-ion recombination rate coefficients of fluorine-like nickel ions were measured at the heavy-ion storage ring CSRm by employing the merged-beams method. The measured rate coefficients agree well with the most recent theoretical calculation by the FAC code, even at very low collision energies. The level-resolved theoretical calculation facilitates the identification of the measured DR resonances. Accordingly, the lowest-energy isolated resonance is associated with the $(2s2p^6[^2S_{1/2}]6s)_{J=1}$ intermediate state. Its experimental resonance position was extracted by a fit to the measured recombination spectrum, resulting in a value of 86 meV with a systemic uncertainty of 2 meV and a fitting error of 2 meV. This accurate measurement of the resonant position in combination with precision theoretical calculations of the binding energy of the $6s$ Rydberg electron enables a precise determination of the $2s^2 2p^5\ ^2P_{3/2} \rightarrow 2s\,2p^6\ ^2S_{1/2}$ core-transition energy. At the present level of experimental accuracy our results are sensitive to third-order correlation and second-order QED effects. The present study establishes precision DR spectroscopy with highly charged ions at the CSRm and paves the way for future precision studies with highly charged ions at the CSRe and the upcoming Heavy Ion Accelerator Facility [85].

ACKNOWLEDGMENTS

This work was funded by the National Key R&D Program of China under Grant No. 2017YFA0402300; the National Natural Science Foundation of China through Grants No. U1932207, No. 11904371, No. 11674066, and No. 12104437; the Strategic Priority Research Program of the Chinese Academy of Sciences Grant No. XDB34020000; and the Heavy Ion Research Facility in Lanzhou (HIRFL). S.X.W. is grateful to the Natural Science Foundation of Anhui Province (Grant No. 2108085QA27) and the Fundamental Research Funds for the Central Universities. W.Q.W. thanks the support from the Youth Innovation Promotion Association of the Chinese Academy of Sciences. A.V.V. acknowledges financial support by the Government of the Russian Federation through the ITMO Fellowship and Professorship Program. The authors would like to thank the CSR accelerator staff for their technical support during the experiment.

[1] M. S. Safronova, D. Budker, D. DeMille, D. F. Jackson Kimball, A. Derevianko, and C. W. Clark, Rev. Mod. Phys. **90**, 025008 (2018).
[2] P. Indelicato, J. Phys. B **52**, 232001 (2019).
[3] P. Beiersdorfer, Can. J. Phys. **87**, 9 (2009).
[4] P. Beiersdorfer, J. Phys. B: At. Mol. Opt. Phys. **43**, 074032 (2010).
[5] M. G. Kozlov, M. S. Safronova, J. R. Crespo López-Urrutia, and P. O. Schmidt, Rev. Mod. Phys. **90**, 045005 (2018).
[6] M. Grieser, Y. Litvinov, R. Raabe, K. Blaum, Y. Blumenfeld, P. A. Butler, F. Wenander, P. J. Woods, M. Aliotta, A. Andreyev, A. Artemyev, D. Atanasov, T. Aumann, D. Balabanski, A. Barzakh, L. Batist, A.-P. Bernardes, D. Bernhardt, J. Billowes, S. Bishop *et al.*, Eur. Phys. J.: Spec. Top. **207**, 1 (2012).
[7] M. Lestinsky, V. Andrianov, B. Aurand, V. Bagnoud, D. Bernhardt, H. Beyer, S. Bishop, K. Blaum, A. Bleile, A. Borovik Jr., F. Bosch, C. J. Bostock, C. Brandau, A. Bräuning-Demian, I. Bray, T. Davinson, B. Ebinger, A. Echler, P. Egelhof, A. Ehresmann *et al.*, Eur. Phys. J.: Spec. Top. **225**, 797 (2016).
[8] M. Steck and Y. A. Litvinov, Prog. Part. Nucl. Phys. **115**, 103811 (2020).
[9] A. Wolf, H. Buhr, M. Grieser, R. von Hahn, M. Lestinsky, E. Lindroth, D. A. Orlov, S. Schippers, and I. F. Schneider, Hyperfine Interact. **172**, 111 (2006).

[10] S. Schippers, Nucl. Instrum. Methods Phys. Res. Sect. B **350**, 61 (2015).

[11] R. Schuch and S. Böhm, J. Phys.: Conf. Ser. **88**, 012002 (2007).

[12] C. Brandau, C. Kozhuharov, A. Müller, D. Bernhardt, D. Banas, F. Bosch, F. J. Currell, C. Dimopoulou, A. Gumberidze, S. Hagmann, P.-M. Hillenbrand, M. Heil, M. Lestinsky, Y. A. Litvinov, R. Märtin, F. Nolden, R. Reuschl, S. Sanjari, S. Schippers, D. Schneider *et al.*, Phys. Scr. **T156**, 014050 (2013).

[13] C. Brandau, C. Kozhuharov, M. Lestinsky, A. Müller, S. Schippers, and T. Stöhlker, Phys. Scr. **T166**, 014022 (2015).

[14] Z. K. Huang, W. Q. Wen, H. B. Wang, X. Xu, L. F. Zhu, X. Y. Chuai, Y. J. Yuan, X. L. Zhu, X. Y. Han, L. J. Mao, J. Li, X. M. Ma, T. L. Yan, J. C. Yang, G. Q. Xiao, J. W. Xia, and X. Ma, Phys. Scr. **T166**, 014023 (2015).

[15] Z. K. Huang, W. Q. Wen, X. Xu, S. Mahmood, S. X. Wang, H. B. Wang, L. J. Dou, N. Khan, N. R. Badnell, S. P. Preval, S. Schippers, T. H. Xu, Y. Yang, K. Yao, W. Q. Xu, X. Y. Chuai, X. L. Zhu, D. M. Zhao, L. J. Mao, X. M. Ma *et al.*, Astrophys. J. Suppl. Series **235**, 2 (2018).

[16] S.-X. Wang, Z.-K. Huang, W.-Q. Wen, C.-Y. Chen, S. Schippers, X. Xu, S. Sardar, N. Khan, H.-B. Wang, L.-J. Dou, S. Mahmood, D.-M. Zhao, X.-L. Zhu, L.-J. Mao, X.-M. Ma, J. Li, M.-T. Tang, R.-S. Mao, D.-Y. Yin, Y.-J. Yuan *et al.*, Astron. Astrophys. **627**, A171 (2019).

[17] T. Stöhlker, P. H. Mokler, K. Beckert, F. Bosch, H. Eickhoff, B. Franzke, M. Jung, Y. Kandler, O. Klepper, C. Kozhuharov, R. Moshammer, F. Nolden, H. Reich, P. Rymuza, P. Spädtke, and M. Steck, Phys. Rev. Lett. **71**, 2184 (1993).

[18] J. R. Crespo López-Urrutia, P. Beiersdorfer, D. W. Savin, and K. Widmann, Phys. Rev. Lett. **77**, 826 (1996).

[19] P. Beiersdorfer, A. L. Osterheld, J. H. Scofield, J. R. Crespo López-Urrutia, and K. Widmann, Phys. Rev. Lett. **80**, 3022 (1998).

[20] T. Stöhlker, P. H. Mokler, F. Bosch, R. W. Dunford, F. Franzke, O. Klepper, C. Kozhuharov, T. Ludziejewski, F. Nolden, H. Reich, P. Rymuza, Z. Stachura, M. Steck, P. Swiat, and A. Warczak, Phys. Rev. Lett. **85**, 3109 (2000).

[21] E. Lindroth, H. Danared, P. Glans, Z. Pesic, M. Tokman, G. Vikor, and R. Schuch, Phys. Rev. Lett. **86**, 5027 (2001).

[22] D. Bernhardt, C. Brandau, Z. Harman, C. Kozhuharov, S. Böhm, F. Bosch, S. Fritzsche, J. Jacobi, S. Kieslich, H. Knopp, F. Nolden, W. Shi, Z. Stachura, M. Steck, T. Stöhlker, S. Schippers, and A. Müller, J. Phys. B: At. Mol. Opt. Phys. **48**, 144008 (2015).

[23] M. Lestinsky, E. Lindroth, D. A. Orlov, E. W. Schmidt, S. Schippers, S. Böhm, C. Brandau, F. Sprenger, A. S. Terekhov, A. Müller, and A. Wolf, Phys. Rev. Lett. **100**, 033001 (2008).

[24] C. Brandau, C. Kozhuharov, A. Müller, W. Shi, S. Schippers, T. Bartsch, S. Böhm, C. Böhme, A. Hoffknecht, H. Knopp, N. Grün, W. Scheid, T. Steih, F. Bosch, B. Franzke, P. H. Mokler, F. Nolden, M. Steck, T. Stöhlker, and Z. Stachura, Phys. Rev. Lett. **91**, 073202 (2003).

[25] D. Bernhardt, C. Brandau, Z. Harman, C. Kozhuharov, S. Böhm, F. Bosch, S. Fritzsche, J. Jacobi, S. Kieslich, H. Knopp, F. Nolden, W. Shi, Z. Stachura, M. Steck, T. Stöhlker, S. Schippers, and A. Müller, Phys. Rev. A **91**, 012710 (2015).

[26] S. Madzunkov, E. Lindroth, N. Eklöw, M. Tokman, A. Paál, and R. Schuch, Phys. Rev. A **65**, 032505 (2002).

[27] S. Kieslich, S. Schippers, W. Shi, A. Müller, G. Gwinner, M. Schnell, A. Wolf, E. Lindroth, and M. Tokman, Phys. Rev. A **70**, 042714 (2004).

[28] A. Müller, Philos. Trans. R. Soc. A **357**, 1279 (1999).

[29] D. A. Orlov, F. Sprenger, M. Lestinsky, U. Weigel, A. S. Terekhov, D. Schwalm, and A. Wolf, J. Phys.: Conf. Ser. **4**, 290 (2005).

[30] A. Kramida, Y. Ralchenko, J. Reader, NIST ASD Team, *NIST Atomic Spectra Database* (Version 5.9. [online]). Available: http://physics.nist.gov/asd, Techical Report (National Institute of Standards and Technology, Washington, D.C., 2021).

[31] G. A. Doschek, U. Feldman, R. D. Cowan, and L. Cohen, Astrophys. J. **188**, 417 (1974).

[32] C. Breton, C. D. Michelis, M. Finkenthal, and M. Mattioli, J. Opt. Soc. Am. **69**, 1652 (1979).

[33] J. Sugar, V. Kaufman, and W. L. Rowan, J. Opt. Soc. Am. B **9**, 344 (1992).

[34] M. F. Gu, At. Data Nucl. Data Tables **89**, 267 (2005).

[35] P. Jönsson, A. Alkauskas, and G. Gaigalas, At. Data Nucl. Data Tables **99**, 431 (2013).

[36] B. K. Nandy and D. K. Sahoo, Astron. Astrophys. **563**, A25 (2014).

[37] R. Si, S. Li, X. L. Guo, Z. B. Chen, T. Brage, P. Jönsson, K. Wang, J. Yan, C. Y. Chen, and Y. M. Zou, Astrophys. J. Suppl. Ser. **227**, 16 (2016).

[38] C. J. Fontes and H. L. Zhang, At. Data Nucl. Data Tables **113**, 293 (2017).

[39] G. Çelik, Ş. Ateş, and S. N. Nahar, Ind. J. Phys. **94**, 565 (2020).

[40] H. W. Zhao, L. T. Sun, J. W. Guo, W. Lu, D. Z. Xie, D. Hitz, X. Z. Zhang, and Y. Yang, Phys. Rev. Accel. Beams **20**, 094801 (2017).

[41] H. Danared, Nucl. Instrum. Methods Phys. Res. Sect. A **335**, 397 (1993).

[42] V. Bocharov, A. Bubley, Y. Boimelstein, V. Veremeenko, V. Voskoboinikov, A. Goncharov, V. Grishanov, A. Dranichnikov, Y. Evtushenko, N. Zapiatkin, M. Zakhvatkin, A. Ivanov, V. Kokoulin, V. Kolmogorov, M. Kondaurov, E. Konstantinov, S. Konstantinov, G. Krainov, A. Kriuchkov, E. Kuper *et al.*, Nucl. Instrum. Methods Phys. Res. Sect. A **532**, 144 (2004).

[43] G. Kilgus, D. Habs, D. Schwalm, A. Wolf, N. R. Badnell, and A. Müller, Phys. Rev. A **46**, 5730 (1992).

[44] H. Poth, Phys. Rep. **196**, 135 (1990).

[45] W. Q. Wen, X. Ma, W. Q. Xu, L. J. Meng, X. L. Zhu, Y. Gao, S. L. Wang, P. J. Zhang, D. M. Zhao, H. P. Liu, L. F. Zhu, X. D. Yang, J. Li, X. M. Ma, T. L. Yan, J. C. Yang, Y. J. Yuan, J. W. Xia, H. S. Xu, and G. Q. Xiao, Nucl. Instrum. Methods Phys. Res. Sect. B **317**, 731 (2013).

[46] J. Wu, Y. Zang, F. Nolden, M. Sanjari, P. Hülsmann, F. Caspers, T. Zhao, M. Li, J. Zhang, J. Li, Y. Zhang, G. Zhu, S. Zhang, X. Ma, H. Xu, J. Yang, J. Xia, R. Mao, and P. Petri, Nucl. Instrum. Methods Phys. Res. Sect. B **317**, 623 (2013).

[47] D. Bernhardt, C. Brandau, Z. Harman, C. Kozhuharov, A. Müller, W. Scheid, S. Schippers, E. W. Schmidt, D. Yu, A. N. Artemyev, I. I. Tupitsyn, S. Böhm, F. Bosch, F. J. Currell, B. Franzke, A. Gumberidze, J. Jacobi, P. H. Mokler, F. Nolden, U. Spillman *et al.*, Phys. Rev. A **83**, 020701(R) (2011).

[48] S. Schippers, T. Bartsch, C. Brandau, A. Müller, G. Gwinner, G. Wissler, M. Beutelspacher, M. Grieser, A. Wolf, and R. A. Phaneuf, Phys. Rev. A **62**, 022708 (2000).

[49] M. F. Gu, Can. J. Phys. **86**, 675 (2008).

[50] M. Wang, G. Audi, A. H. Wapstra, F. G. Kondev, M. MacCormick, X. Xu, and B. Pfeiffer, Chin. Phys. C **36**, 1603 (2012).

[51] E. Tiesinga, P. J. Mohr, D. B. Newell, and B. N. Taylor, Rev. Mod. Phys. **93**, 025010 (2021).

[52] W. Shi, T. Bartsch, C. Böhme, C. Brandau, A. Hoffknecht, H. Knopp, S. Schippers, A. Müller, C. Kozhuharov, K. Beckert, F. Bosch, B. Franzke, P. H. Mokler, F. Nolden, M. Steck, T. Stöhlker, and Z. Stachura, Phys. Rev. A **66**, 022718 (2002).

[53] C. Froese Fischer, G. Gaigalas, P. Jönsson, and J. Bieroń, Comput. Phys. Commun. **237**, 184 (2019).

[54] I. P. Grant, *Relativistic Quantum Theory of Atoms and Molecules: Theory and Computation* (Springer, New York, 2007).

[55] J. P. Desclaux, Comput. Phys. Commun. **9**, 31 (1975).

[56] Y. K. Ho, Phys. Rep. **99**, 1 (1983).

[57] B. I. Schneider, J. Phys.: Conf. Ser. **759**, 012002 (2016).

[58] A. U. Hazi and H. S. Taylor, Phys. Rev. A **1**, 1109 (1970).

[59] M. F. Fels and A. U. Hazi, Phys. Rev. A **4**, 662 (1971).

[60] J. Müller, X. Yang, and J. Burgdörfer, Phys. Rev. A **49**, 2470 (1994).

[61] S. Kar and Y. K. Ho, Phys. Rev. A **72**, 010703(R) (2005).

[62] J. K. Saha and T. K. Mukherjee, Phys. Rev. A **80**, 022513 (2009).

[63] P. Amaro, J. P. Santos, S. Bhattacharyya, T. K. Mukherjee, and J. K. Saha, Phys. Rev. A **103**, 012811 (2021).

[64] V. A. Mandelshtam, T. R. Ravuri, and H. S. Taylor, Phys. Rev. Lett. **70**, 1932 (1993).

[65] I. I. Tupitsyn, V. M. Shabaev, J. R. Crespo López-Urrutia, I. Draganić, R. Soria Orts, and J. Ullrich, Phys. Rev. A **68**, 022511 (2003).

[66] I. I. Tupitsyn, A. V. Volotka, D. A. Glazov, V. M. Shabaev, G. Plunien, J. R. Crespo López-Urrutia, A. Lapierre, and J. Ullrich, Phys. Rev. A **72**, 062503(R) (2005).

[67] M. Y. Kaygorodov, Y. S. Kozhedub, I. I. Tupitsyn, A. V. Malyshev, D. A. Glazov, G. Plunien, and V. M. Shabaev, Phys. Rev. A **99**, 032505 (2019).

[68] W. H. Furry, Phys. Rev. **81**, 115 (1951).

[69] A. V. Volotka, M. Bilal, R. Beerwerth, X. Ma, T. Stöhlker, and S. Fritzsche, Phys. Rev. A **100**, 010502(R) (2019).

[70] V. M. Shabaev, I. I. Tupitsyn, M. Y. Kaygorodov, Y. S. Kozhedub, A. V. Malyshev, and D. V. Mironova, Phys. Rev. A **101**, 052502 (2020).

[71] G. O'Neil, S. Sanders, P. Szypryt, Dipti, A. Gall, Y. Yang, S. M. Brewer, R. Doriese, J. Fowler, A. Naing, D. Swetz, J. Tan, J. Ullom, A. V. Volotka, E. Takacs, and Y. Ralchenko, Phys. Rev. A **102**, 032803 (2020).

[72] Q. Lu, C. L. Yan, G. Q. Xu, N. Fu, Y. Yang, Y. Zou, A. V. Volotka, J. Xiao, N. Nakamura, and R. Hutton, Phys. Rev. A **102**, 042817 (2020).

[73] V. M. Shabaev, Phys. Rep. **356**, 119 (2002).

[74] P. J. Mohr, G. Plunien, and G. Soff, Phys. Rep. **293**, 227 (1998).

[75] Y. S. Kozhedub, A. V. Volotka, A. N. Artemyev, D. A. Glazov, G. Plunien, V. M. Shabaev, I. I. Tupitsyn, and T. Stöhlker, Phys. Rev. A **81**, 042513 (2010).

[76] A. V. Malyshev, A. V. Volotka, D. A. Glazov, I. I. Tupitsyn, V. M. Shabaev, and G. Plunien, Phys. Rev. A **90**, 062517 (2014).

[77] A. V. Malyshev, A. V. Volotka, D. A. Glazov, I. I. Tupitsyn, V. M. Shabaev, and G. Plunien, Phys. Rev. A **92**, 012514 (2015).

[78] V. A. Yerokhin and V. M. Shabaev, J. Phys. Chem. Ref. Data **44**, 033103 (2015).

[79] V. Shabaev, Theor. Math. Phys. **63**, 588 (1985).

[80] V. Shabaev, Sov. J. Nucl. Phys. **47**, 107 (1988).

[81] C. W. P. Palmer, J. Phys. B **20**, 5987 (1987).

[82] V. M. Shabaev and A. N. Artemyev, J. Phys. B: At. Mol. Opt. Phys. **27**, 1307 (1994).

[83] S. Schippers, M. Schnell, C. Brandau, S. Kieslich, A. Müller, and A. Wolf, Astron. Astrophys. **421**, 1185 (2004).

[84] H. A. Bethe and E. E. Salpeter, *Quantum Mechanics of One- and Two-Electron Atoms* (Springer Science & Business Media, New York, 2012).

[85] X. Ma, W. Wen, S. Zhang, D. Yu, R. Cheng, J. Yang, Z. Huang, H. Wang, X. Zhu, X. Cai, Y. Zhao, L. Mao, J. Yang, X. Zhou, H. Xu, Y. Yuan, J. Xia, H. Zhao, G. Xiao, and W. Zhan, Nucl. Instrum. Methods Phys. Res. Sect. B **408**, 169 (2017).